Editors' Suggestion

Autonomous multi-ion optical clock with on-chip integrated photonic light delivery

Tharon D. Morrison,[1,*,†] Joonhyuk Kwon,[1,*,‡] Matthew A. Delaney,[1] Michael Gehl,[1] David R. Leibrandt,[2] Daniel Stick,[1,3] and Hayden J. McGuinness[1,4]

[1]*Sandia National Laboratories, Albuquerque, New Mexico, 87185, USA*
[2]*Department of Physics and Astronomy, University of California, Los Angeles, California, 90095, USA*
[3]*Present address: IonQ Inc., College Park, Maryland USA*
[4]*Present address: Quantinuum, Broomfield, Colorado, USA*

(Received 23 January 2026; revised 17 June 2026; accepted 5 October 2026; published 13 November 2026)

Integrated photonics in trapped-ion systems are critical for applications such as portable optical atomic clocks and scalable quantum computers. System-level integration of all required functionalities remains a key challenge. In this work, we demonstrate an autonomously operating optical clock having a short-term frequency instability of $3.14(5) \times 10^{-14}/\sqrt{\tau}$ using an ensemble of four $^{171}Yb^{+}$ ions trapped in a multisite surface-electrode trap at room temperature. All clock operations are performed with light delivered via on-chip waveguides. We showcase the system's resilience through sustained, autonomous operation featuring automated ion shuttling and reloading to mitigate ion loss during interleaved clock measurements. This work paves the way beyond component-level functionality to establish a viable and robust architecture for the next generation of portable, multi-ion quantum sensors and computers.

DOI: 10.1103/6tt6-vpf2

I. INTRODUCTION

As time and frequency standards, optical atomic clocks offer unparalleled precision for applications in fundamental physics [1–6], navigation [7], and telecommunications [8,9]. Those based on neutral atoms trapped in an optical lattice provide high precision and accuracy [10–13] but contain complex atom-atom interactions and require large high-power laser systems and atomic ovens. In contrast, trapped-ion clocks [4,14,15] provide excellent isolation of individual ions with minimal disturbance of internal states. However, the comparatively small number of ions limits the quantum projection noise. Both platforms typically rely on bulky optical components, which limit their operation to laboratory environments.

The path to deploying these instruments outside of the laboratory lies in miniaturization and ruggedization [7,16], a challenge for which integrated photonics provides a compelling solution. By replicating complex optical functionalities on scalable chip-based platforms [17,18], this approach works to reduce the system's footprint and to enable advanced multi-ion architectures that are less practical with conventional optics [19–21]. The replacement of complex free-space optics with on-chip waveguides and splitters [22–24], grating couplers [25–27], and photonic control [28] provides robust and scalable delivery of the multiple laser wavelengths required for narrow transition control. These technologies are also applicable to trapped-ion quantum computing, notably the quantum charge-coupled device (QCCD) architecture [29,30], which requires multiplexed operations and coherent control across many distinct trapping zones [31]. By providing a pathway to individually address dense ion arrays, integrated photonics are critical for moving beyond small-scale experiments, toward large-scale quantum platforms.

Recently demonstrated building blocks for this architecture include simultaneous multisite optical addressing [24] and coherent transport of ions between zones [31]. These demonstrations are complemented by broader efforts extending multizone operation and integrated photonic delivery in ion traps [32–34]. Although these advances are foundational, they have focused on individual capabilities rather than their combination into a unified application-focused system. Complementing these efforts in ion trap integration, there is parallel progress developing high-stability, chip-scale lasers, and on-chip frequency combs for integrated, high-performance light sources [35,36], as well as integrated semiconductor detectors [37,38] and superconducting nanowire single-photon detectors for state readout [39].

In this work, we bridge the application gap by demonstrating an optical clock using an ensemble of up to four

*These authors contributed equally to this work.
†Contact author: tdmorr@sandia.gov
‡Contact author: jookwon@sandia.gov

Published by the American Physical Society under the terms of the Creative Commons Attribution 4.0 International license. Further distribution of this work must maintain attribution to the author(s) and the published article's title, journal citation, and DOI.

$^{171}Yb^{+}$ ions in a room-temperature, multisite, integrated photonics trap. All stages of the clock sequence—state preparation, coherent qubit manipulation, and detection—are performed using light delivered entirely by on-chip waveguides. The significance of this achievement lies not in the raw clock performance but in the successful system-level integration of all operational stages, from automated ion loading and shuttling to interleaved clock interrogation. The realization of this system required overcoming significant practical challenges, including managing on-chip waveguide scattering and optimizing ion placement to balance performance trade-offs across multiple sites. This demonstration of sustained operation despite ion loss moves beyond component-level functionality and establishes an architecture for the next generation of portable, scalable, multi-ion quantum sensors and quantum computing systems.

II. RESULTS

A. Experimental setup

In previous demonstrations of integrated photonic ion traps, we used a free-space grating input coupling scheme [24,40]. This technique suffered from low coupling efficiency and poor stability. The performance of both was improved here by directly coupling an array of fibers to the trap. Single-mode, polarization-maintaining fibers in Pyrex v-groove arrays (VGAs) [41] were aligned with a matching array of tapered waveguides at the edge of the trap chip. Each beam was split via multimode interferometer (MMI) splitters into five waveguides, which were directed to separate clock sites. Each site was addressable with four waveguide output grating windows that delivered light at 369, 435, 935, and 760 nm. Figure 1(a) shows an illustration of the site layout on the chip. The optical loss in each waveguide path was primarily due to imperfect input coupling, material absorption, scattering during propagation, and diffraction inefficiency. The total loss for the probe beam (435 nm) was −27 dB; although it is difficult to identify the contribution of each loss mechanism, measurements from the loop-back optimization suggest that most of the loss is due to the fiber-to-trap coupling.

For this work, we used the 435 nm E2 (clock) transition of $^{171}Yb^{+}$. This additionally requires 369 nm for Doppler cooling and detection and 935 nm for repump and state preparation. A 760 nm beam can be used to pump the $^{2}F_{7/2}$ state to $^{1}[3/2]_{3/2}$ to rejoin the Doppler cooling cycle [42]; however, in our systems, it does not significantly improve the overall lifetime of the ions [24].

New ions are loaded from sublimated ^{171}Yb vapor produced by an oven that was powered on and off during clock operation. Resonant 399 nm and nonresonant 393 nm beams photoionized a fraction of the vapor, producing ions that could then be trapped in the rf and dc confining fields generated by voltages applied to the trap electrodes. Due to the power requirements of the 393 beam and the losses from the fiber-to-trap coupling, a free-space beam launch that also included the Doppler and repump beam was used for loading. As a proof-of-principle demonstration, loading via waveguide-delivered cooling and repump beams was demonstrated on separate occasions, but with free-space 393 and 399 nm beams. All clock algorithm lasers were delivered to the ions via integrated waveguides and output grating. State detection fluorescence was collected via a side-imaging system. The low numerical aperture (NA) geometry limits the overall detection time (see Appendix).

All dc electrodes were individually controlled such that the trapping potential of an individual ion at each site could

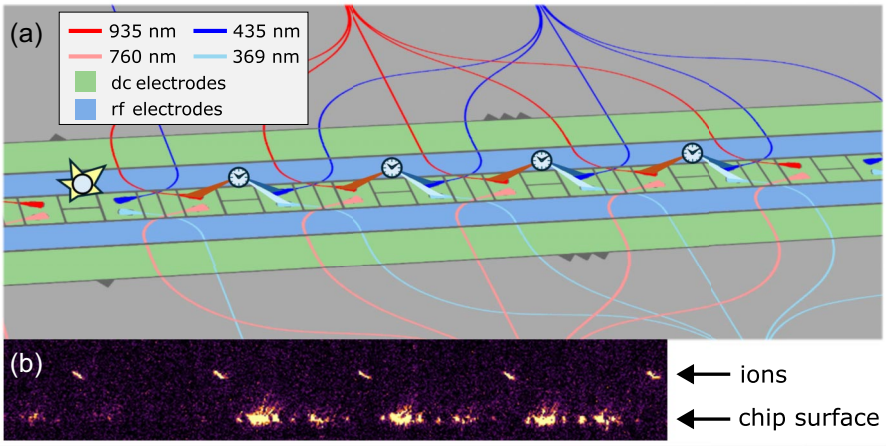


FIG. 1. Schematic image of the integrated multi-ion trap. (a) Illustration of trapped ions above the surface of the integrated waveguide chip, with the loading site indicated by the star-burst and the clock sites indicated by clock icons. The trapping regions include waveguides on two different embedded layers (reds and blues) and dc electrodes (green) and rf electrodes (teal) on the top layer. (b) Camera view of trapped ions. As a check, ions are aligned via camera prior to fine alignment with a multichannel PMT array. Ions are imaged from the side to reduce background from scattered light.

be compensated with minimal effect on a neighboring site. When an ion is loaded, it is adiabatically transported to a vacant clock site without extended delays to limit motional heating. Since each beam has its own axis of emission, the beam overlap is determined by the design and lithography of the diffraction gratings, as are the individual beam intensity distributions. Due to small imperfections in the beam overlap, there was a compromise between fluorescent counts (requiring good 369 and 935 nm beam overlap), the E2 transition Rabi frequency, and the coherence time (efficient cooling versus excess heating). The dc electrodes were tuned to position the ions at each clock site to achieve similar values for these quantities across all sites and place the ions near the rf null. The axial trapping frequency defined by the dc potential was 1.02 MHz, and the radial trapping frequencies defined by the rf voltage were 3.06 and 3.11 MHz. The dc voltages applied to maintain this compromise did not vary from day to day. However, there were variations correlated with the applied 369 nm beam power. We hypothesize that this is due to charging of the dielectric of the output grating windows. When 369 nm power was altered, the correction voltages would often take a few hours to settle. If the 369 nm power was returned to nominal values, the voltage corrections would also return to the nominal values on a similar timescale.

B. Clock protocol for multi-ion ensemble operation

The clock utilizes a Rabi interrogation scheme with the pulse sequence shown in Fig. 2(a). All ions are Doppler cooled (2 ms) and undergo state preparation (30 μs). Then, the ensemble of ions is probed on the E2 transition, $|^2S_{1/2}, F = 0, m_F = 0\rangle \rightarrow |^2D_{3/2}, F = 2, m_F = 0\rangle$, for ($T_{\text{probe}} = 800$ μs). This probe occurs at half its spectroscopic width on either side of the inferred center. For this experiment, two separate servos track the frequency to determine the fractional frequency instability. Probing at the half-width yields a 50% probability that the ion is not shelved in the clock state and subsequently appears bright during detection (3 ms). This choice also provides a large derivative of bright detection with detuning of the center frequency to form the error signal. This method is similar to [43]; however, the feedback receives input from the "j"th ion in the ensemble each clock cycle. We denote the individual bright ions as "1" and dark ions as "0". During a clock cycle, each servo tracks its own interrogations, denoted n_{ijS}, where i indicates the servo (1 or 2) and S is either $+$ or $-$ its center frequency by half the spectral width. The servo comprises two integrator stages. The imbalance $(n_+ - n_-)$ is added to the first-order integrator, and the second-order integrator is incremented by the first order. Together and in-order, these steps are as follows:

$$\begin{aligned} I_i^{(2)} &+= I_i^{(1)} \\ I_i^{(1)} &+= \sum_j n_{ij+} - n_{ij-}. \end{aligned} \tag{1}$$

The total frequency displacement of each servo (Δf_i) to track the optical resonance of the clock transition is

$$\Delta f_i = \left(g^{(1)} I_i^{(1)} + g^{(2)} I_i^{(2)}\right) \times \text{FWHM}, \tag{2}$$

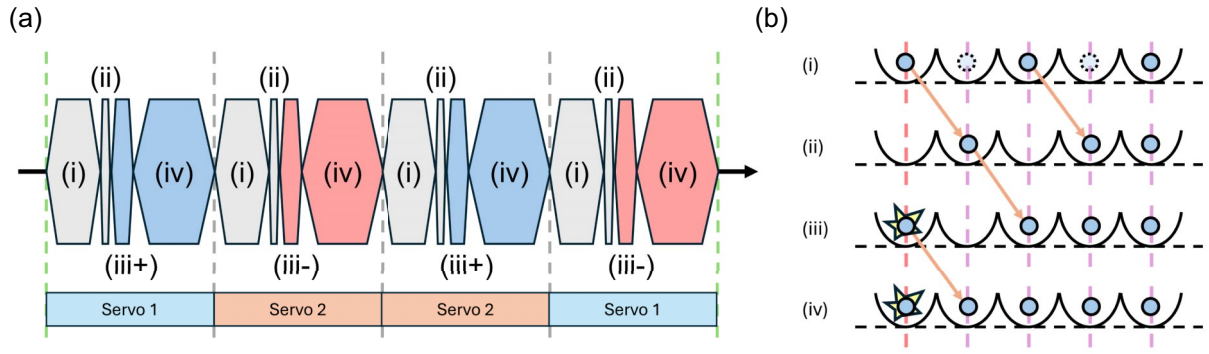


FIG. 2. Multi-ion clock protocol. (a) Pulse sequence used in the interleaved clock measurement. The sequence involves Doppler cooling (i) immediately followed by state preparation (ii). The ions are then probed (iii) using a servo's inferred center either plus (+) or minus (−) half of the previously measured spectroscopic linewidth. The detection beams are then applied (iv) to determine if shelving in the $^2D_{3/2}$ state was successful. The servo used for the probe and readout is labeled under the pulse sequence (this marks T_S discussed in Sec. II C). Because the waveguide equally distributes light to all output waveguides in the ensemble, all clock sites are probed simultaneously independent of whether an ion is present or not. The green vertical lines indicate when the algorithm updates the center frequency of each servo (T_{cycle}). Every 20 center frequency updates, requests for new ions are made to sites with insufficiently bright detection outcomes. (b) Cartoon depicting the refill procedure that occurs as the clock is running. When the requests for new ions are made, multiple ions can be lost simultaneously. The farthest sites from the loading site are preferentially filled first. To refill remaining sites, new ions are trapped at a loading site (red, dashed vertical line) and shuttled to clock sites (purple, dashed vertical lines). The starburst indicates the loading of a new ion.

where $g^{(1)}$ is a first-order gain (approximately 10^{-3}) and $g^{(2)}$ is a second-order gain (approximately 10^{-6}). The sign of the gain mediates the acousto-optic modulator (AOM) diffraction order used to apply the shift. FWHM is the spectral full-width at half-maximum measured before starting. In our experiment, this approaches the transform-limited FWHM given by the probe time. Differences in the frequency displacement, $\pm(\Delta f_1 - \Delta f_2)$ plus an offset (the resonant frequency of the AOM) plus or minus half the spectral width is then applied by a double-pass AOM to the local oscillator light for the next interrogation. Common-mode drift in the frequency displacement $(\Delta f_1 + \Delta f_2)$ is applied to a second double-pass AOM shifting the local oscillator with respect to the Ultra-Low Expansion (ULE) cavity to which it is stabilized. The interleaved comparison of two different servos track independent interrogations, resulting in separately inferred frequency displacements. The frequency displacement difference, $\Delta f_1 - \Delta f_2$, is used to determine the frequency instability in the next section.

In addition to managing the servo feedback, the measurement also informs which ions are still present. To determine whether an ion is present, the number of bright measurement outcomes for each ion is tracked, $p_j = \sum_i \sum_S n_{ijS}$. Ions that appear dark fall into one of three categories: (1) shelved in the clock state, (2) collisionally excited to another internal state, and (3) physically lost from the trapping potentials. Due to our clock scheme, the ion will not be shelved approximately 50% of the time. However, when an ion is lost, the bright probability goes to 0. The shuttling software receives a report every 20 clock cycles indicating the trap sites, if any, in need of refilling. Given this reporting rate, the threshold for a lost ion is $p_j \leq 5 \approx 0.5 \times 20 - \sqrt{20}$. The reporting rate is limited by the rate at which the shuttling software can communicate consistently with the DAC responsible for the dc trapping potentials. The remaining ions are shuttled into vacancies, automatically filling the farthest clock sites from the loading site first. An ion is also stored at the loading site as a buffer to quickly replenish empty clock sites. In cases where multiple ions are lost, a new ion will be loaded while the clock runs and replenished as soon as it becomes available. An illustration of this can be seen in Fig. 2(b). The ion lifetime on a site-specific basis was correlated with the distance from the loading site. This motivated filling the farthest sites first. One hypothesis for this effect is that the localized pressure associated with neutral flux and heated surfaces increases the rate of collisions, reducing lifetimes. The ion lifetimes were approximately 15 min when individual ions were trapped and cooled, but were reduced to one minute during clock operation, further supporting this hypothesis. Feedback occurs as long as any ions remain. Despite these short lifetimes, we were able to keep the clock sites fully occupied with four ions for more than 45% of the time. Furthermore, we operated the clock system continuously for more than two hours on multiple occasions. Algorithmic interlocks predominantly limited the duration in these cases. The interlocks halted the clock operation where the ions became difficult to trap or there were no ions in any sites for an extended period of time due to lasers unlocking. This attests to the effectiveness of the automated ion reloading, shuttling, and clock-cycle reintegration capabilities of the system.

C. Frequency stability of integrated photonics multi-ion clock

Figure 3 shows the performance of the integrated photonics 4-ion ensemble clock. The expected quantum projection noise (QPN) of a single servo is calculated as follows [44]:

$$\sigma_{\mathrm{QPN}}(\tau) = \frac{1.66}{2\pi\nu C T_{\mathrm{probe}}} \sqrt{\frac{T_{\mathrm{cycle}}}{N m \tau}}, \tag{3}$$

where ν is the transition frequency, C is the spectroscopic contrast, T_{probe} is the time the transition frequency is measured, T_{cycle} is the total cycle time, N is the number of ions probed, m is the number of probes that occur during T_{cycle} that contribute to a servo, and τ is the averaging time. The factor of 1.66 comes from the Rabi probe scheme [44]. The expected fractional frequency instability limited by the quantum projection noise is calculated, assuming that all ions are always present ($N = 4$). Additionally, a servo interrogates the "+" and "−" sides of the transition during T_{cycle}, enforcing $m = 2$. Each interrogation includes cooling, state preparation, probing the clock transition, and detection in total time T_S. The total cycle time is four side interrogations for the interleaved measurement

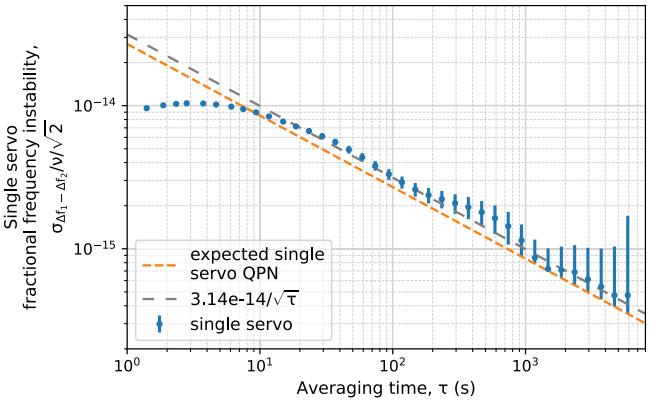


FIG. 3. Allan deviation. Single-servo fractional frequency instability. The fit line of $3.14(5) \times 10^{-14}/\sqrt{\tau}$ is plotted in gray. The expected quantum projection noise of 4 ions and a T_{cycle} of four side interrogations is plotted in orange. Fractional frequency stability for averaging times less than 20 s is outside of the servo-bandwidth limited by the combined stability of the local oscillator and its referenced ULE cavity.

($T_{\text{cycle}} = 4T_S$) and corresponds to the distance between the dashed green lines in Fig. 2(a). Finally, the quantum projection noise of the individual servos sums in quadrature for the interleaved frequency differences ($\sigma^2_{\Delta f_1 - \Delta f_2} = \sigma^2_{\Delta f_1} + \sigma^2_{\Delta f_2}$). Assuming that both servos have the same instability, we report a single-servo clock with a short-term fractional frequency instability $\sigma_{\Delta f_1 - \Delta f_2}/\nu/\sqrt{2} = 3.14(5) \times 10^{-14}/\sqrt{\tau}$ and expected quantum projection noise instability ($T_{\text{cycle}} = 4T_S$, $N = 4$) of $2.70 \times 10^{-14}/\sqrt{\tau}$ for an individual clock.

These comparisons demonstrate that the clock performs within a factor of two of the expected quantum projection noise. The deviation is likely caused by technical noise sources. Ion number fluctuations during the experiment would also limit the ability to reach the QPN limit, e.g., the expected quantum projection noise instability for ($T_{\text{cycle}} = 4T_S$, $N = 3$) is $3.1 \times 10^{-14}/\sqrt{\tau}$. If we were to operate a clock with all interrogations used to update a single servo, the update cycle would be improved by a factor of two, $T_{\text{cycle}} = 2T_S$. The resulting clock would have an expected fractional frequency instability of $2.2 \times 10^{-14}/\sqrt{\tau}$ and a quantum projection noise instability ($T_{\text{cycle}} = 2T_S$, $N = 4$) of $1.9 \times 10^{-14}/\sqrt{\tau}$. We were unable to directly measure the single-servo clock stability because we did not have access to a frequency reference with sufficient stability.

D. Characterization of uniformity for future scalability

Site uniformity is of great interest to scalable designs for atomic clocks, quantum sensors, and quantum computation, more broadly. Small shifts in the clock transition can lead to absolute frequency and gate errors. Efforts to calibrate for site-specific differences work on a small scale, but the number of calibrations becomes more tedious and the maintenance becomes intractable as the number of sites grows. Therefore, it is desirable to achieve general uniformity across all sites.

The direction and focal size of each waveguide output beam is lithographically defined to be at the same spot and approximately 6 μm in diameter. Before running the clock algorithm, the ions were verified to have similar counts, Rabi frequencies, and coherence times. The electrodes must be finely tuned to match these, as small local differences are hard to predict. As mentioned previously, we observed a dependence of the compensation voltages on the 369 nm beam power. Because the timescale of the effect was hours, the small periods of the 369 nm beam being off were inconsequential [step iii in Fig. 2(a)]. Once established, the compensations would hold for several weeks. The 369 power drift did not become consequential unless changed by a factor of 2 or more. Figure 4(a) shows a representative set of Rabi flops from an ion at each site. Measurements are modeled similarly to [45]. The ions are trapped in separate dc potentials 180 μm apart, so the chain configuration terms can be dropped, resulting in the following equation for the probability of each ion being shelved in the clock state:

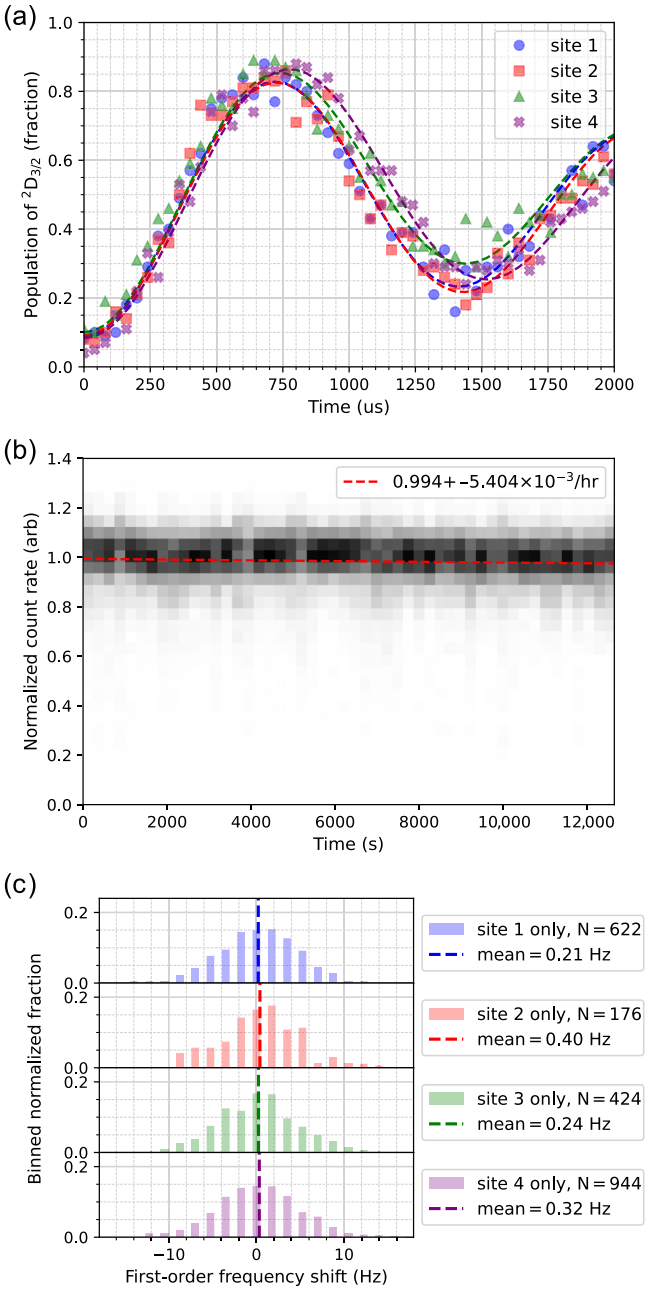


FIG. 4. Uniformity. (a) Representative Rabi flops. Ion positions in the waveguide beams are tuned using dc electrodes to achieve Rabi flops with similar features. Fit parameters according to Eq. (4) are listed in Table I. (b) Ion number normalized count rate during clock operation. The count rate is influenced by changes in 369 beam power, clock transition broadening mechanisms, and ion position fluctuation. (c) First-order frequency shifts for single-ion data. For this data, only one of the clock sites is occupied. Each mean is consistent with zero.

TABLE I. Fit parameters to Eq. (4) for representative Rabi flops in Fig. 4(a). The secular trapping frequencies for this experiment were 1.02, 3.06, and 3.11 MHz. The lower axial frequency was used for the secular frequency in the defined value of η to form a conservative estimate of $\bar{n}$, despite the laser projecting partially onto all motional modes.

Site	A	$\Omega_0/2\pi$ (Hz)	$\bar{n}$	c
1	0.80(4)	796(9)	28(3)	0.09(2)
2	0.78(4)	783(10)	25(3)	0.09(2)
3	0.85(5)	796(10)	37(4)	0.10(2)
4	0.86(3)	746(7)	31(3)	0.08(2)

$$P(t) = c + \frac{A}{2} \times \left[1 - \mathrm{Re}\left(\frac{e^{i\Omega_0 t} e^{-i\Omega_0 \eta^2 t/2}\left(1 - \frac{\bar{n} e^{i\Omega_0 \eta^2 t}}{\bar{n}+1}\right)}{(\bar{n}+1) - 2\bar{n}\cos(\Omega_0 \eta^2 t) + \frac{\bar{n}}{\bar{n}+1}}\right)\right], \tag{4}$$

where A and c determine our spectroscopic contrast, Ω_0 is the Rabi frequency, $\eta = \frac{1}{\lambda}\sqrt{\frac{h}{2mf_{\mathrm{sec}}}}$, and $\bar{n}$ is the average occupation of the corresponding secular motion. η is defined prior to fitting by choice of secular frequency (f_{sec}), species mass (m), and transition wavelength (λ). The bias is added to the fit to account for stray photons that scatter into the PMT. Individual trace fit values are shown in Table I.

By normalizing the bright counts to the number of ions identified in the system, we show that the fluorescent count rate is stable across the entire run. The fluctuations are due to the lack of a power servo on the 369 and 435 nm beams, additional broadening mechanisms that alter the placement of the half spectral width probe on the lineshape, and changes in the ion position that affect the intensity of the beams on the ions. A free-space system would experience these same bright count drift mechanisms while also being subject to the mechanical creep of conventional optics. Based on this analysis, we lose less than 2% of the bright count rate, indicating that this system is at least as stable as free-space systems without a power servo.

During the clock protocol, and as part of the shuttling procedure, the algorithm reports which ions are present. This allows for the extraction of site-specific shifts during postprocessing. To analyze the site-specific shift, we define a related quantity, the first-order frequency shift:

$$\Delta f_i^{(1)} = \sum_j g^{(1)}(s_{ij+} - s_{ij-}) \times \mathrm{FWHM}. \tag{5}$$

Only the first-order is considered because the full servo continues to steer the overall frequency. This is then binned by the ions present in that reporting period. Figure 4(c) shows the first-order frequency shift constrained to only one ion at a specific site. These data are sparse but are most sensitive to localized site-specific shifts. Due to the average occupancy of the ensemble, these points are also predominately flanked by reporting periods containing two or more ions. Based on this analysis, if a site-specific shift exists, it is below the first-order servo error of our system (1.75 Hz) and statistically consistent with no shift between sites during the experiment.

III. OUTLOOK

In this work, we present an autonomously operating, trapped-ion optical clock built on a multisite integrated photonics chip with an ensemble of $^{171}Yb^{+}$ ions. The fractional frequency instability of the resulting clock is $3.14(5) \times 10^{-14}/\sqrt{\tau}$. We also demonstrate that individual sites do not exhibit clock transition frequency differences greater than the first-order servo error of 1.75 Hz. This marks a milestone for the realization of scalable photonic ion traps for clocks, sensors, and quantum computation.

Near-term improvements include the vacuum pressure, which has gradually degraded as a result of tiny leaks in the fiber feedthroughs and out-gassing from the epoxy coated acrylite fibers. These materials do not meet the highly restrictive out-gassing standards required to achieve significantly longer lifetimes. With a better choice of UHV materials, an improved vacuum will extend the ion lifetime by preventing collision-induced loss and micromotion. The reduced collisional decoherence should also allow us to further lower the quantum projection noise by using longer Ramsey sequences for interrogation instead of Rabi pulses.

This trap suffers from high heating rates (10 quanta/ms). Although this was not likely the limiting factor in clock performance, future systems with improved detection efficiency and ion lifetime would benefit from cooler atoms and the associated improved contrast and coherence time. One culprit for high heating rates could be noise due to the buildup of charge on the dielectric surfaces of the grating windows [46]. This could be alleviated by a conductive but transparent coating over the grating windows, such as indium-tin-oxide. In addition, side-band cooling was not implemented. Side-band cooling was time prohibitive, in part because of the low optical coupling from fiber-to-trap. Better optical coupling would allow for side-band cooling and increase both contrast and coherence time.

The ion lifetime while operating the clock was shorter than most of our other systems and ultimately impacted the clock stability. However, by implementing a technique to automatically load and shuttle ions while simultaneously performing interrogations, we demonstrated the robustness of the approach. The fact that no lapse in clock operation occurred is critical and is directly beneficial for various applications. Moreover, since the protocol used in this work can be scaled to use many ions arranged in multiple

ensembles, we believe that this approach using high levels of integration at the chip level can support both more accurate and more deployable atomic clocks for future metrological and sensing applications.

ACKNOWLEDGMENTS

Sandia National Laboratories is a multi-mission laboratory managed and operated by National Technology & Engineering Solutions of Sandia, LLC (NTESS), a wholly owned subsidiary of Honeywell International Inc., for the U.S. Department of Energy's National Nuclear Security Administration (DOE/NNSA) under Contract DE-NA0003525. This written work is authored by an employee of NTESS. The employee, not NTESS, owns the right, title, and interest in and to the written work and is responsible for its contents. Any subjective views or opinions that might be expressed in the written work do not necessarily represent the views of the U.S. Government. The publisher acknowledges that the U.S. Government retains a nonexclusive, paid-up, irrevocable, world-wide license to publish or reproduce the published form of this written work or allow others to do so, for U.S. Government purposes. The DOE will provide public access to results of federally sponsored research in accordance with the DOE Public Access Plan. This work was supported in part by the Laboratory Directed Research and Development program at Sandia National Laboratories; DOE Office of Science; the U.S. Department of Energy Office of Science National Quantum Information Science Research Centers, Quantum Systems Accelerator; and the Defense Advanced Research Projects Agency (DARPA). D.R.L. was supported in part by the National Science Foundation Q-SEnSE Quantum Leap Challenge Institute (Grant No. OMA-2016244).

DATA AVAILABILITY

Data has been made available [47].

APPENDIX A: EXPERIMENTAL SYSTEM

1. Trap design, fabrication, and vacuum

The experiment was conducted using a trap designed and fabricated at Sandia National Laboratories. Although this trap shares features with previous designs [24,40], it uniquely incorporates a 1×5 multimode interferometer (MMI) waveguide splitter for simultaneous multi-ion clock interrogation. $^{171}Yb^{+}$ is a good species for deployable and robust systems due to the E2 transition being first-order Zeeman insensitive. The large wavelength range required to address $^{171}Yb^{+}$ (369 to 935 nm) adds to the design complexity. Shorter wavelengths require unique waveguide designs and are more sensitive to fabrication tolerances and feature roughness. All waveguides, including 369 and 435 nm, were made with silicon nitride using a plasma-enhanced chemical vapor deposition nitride film that Sandia National Laboratories optimized for low propagation loss at blue and UV wavelengths.

Fiber v-groove arrays (VGAs) by Optelligent were attached to the silicon trap chip using UHV vacuum-compatible glue. Single-mode polarization-maintaining fibers of the appropriate core diameters (to ensure single-mode propagation at the appropriate wavelength) were placed in Pyrex v-groove arrays prior to attaching [31]. The assemblies were aligned to matching arrays of tapered waveguides on the edge of the trap chip. These tapered waveguide array edge-couplers were pointed perpendicularly to the trap axis to minimize scattering into the readout optics. The attachment was optimized by maximizing the light that circulates through an additional on-chip loop-back waveguide. For a fiber feedthrough, holes large enough to fit several fibers were drilled through a 2.75-inch CF flange. The fibers were inserted and epoxied in place using low out-gassing 3 M Scotch-Weld 2216 epoxy.

The on-trap MMI splits a single input for each beam into five waveguides, which go to separate clock sites 180 μm apart. Although there are five sites per splitter, only four are used for clock operation. The specific trap used in this system had several malfunctioning electrodes at the fifth site, making that site functionally inoperable for tuning. Due to the same electrodes, shuttling past this site to access a farther ensemble of clock sites was frequently unsuccessful and deemed not useful in a experiment.

2. Ion trapping and shuttling

Vaporized ytterbium atoms are provided through a loading slot, roughly $2\ \mu m \times 22\ \mu m$, which penetrates through the trap electrodes and substrate. By applying a current to an oven containing ytterbium metal located a few centimeters below the loading site, a sufficient neutral vapor for loading is generated. A two-photon process using 399 nm (resonant) and 393 nm (nonresonant) lasers photoionizes the neutral ytterbium. It is important to note that these beams are only used for ionization and not for operations involving the clock algorithm. Due to its nonresonant nature and high power requirement, the 393 nm beam was delivered via a free-space launch; the 399 nm beam was combined with it for simplicity. The necessary Doppler and repump beams for the loading site were also delivered via free-space, which proved helpful for diagnostic purposes. The loading site also has its own set of waveguides (without an MMI splitter), which require approximately five times less power to operate than the clock site waveguides. Waveguide-based loading was demonstrated on a separate occasion. In both cases, the ions typically load in tens of seconds.

The dc and rf fields provided by the trap electrodes confine the newly ionized atom at the loading site when

laser cooled. The rf field is driven at approximately 40 MHz to confine the ion radially with trapping frequencies near 3.1 MHz. Dc fields confine ions axially with a trapping frequency of 1.02 MHz. Rf power was monitored by a Texas Instruments LMH2120 power detector chip with a 1% capacitive pick-off circuit between the helical resonator and the trap rf input and was used in a servo to maintain constant rf power. The trapping pseudopotential defined by the rf field holds ions approximately 50 μm above the electrode surface, where all waveguide beams are designed to converge at their focuses at the interrogation sites. We measure an average motional quanta of $\bar{n} \sim 30$ quanta based on the fitting of Rabi oscillations [45] with a detection fidelity of 87%, which is comparable to previous research [24]. This low detection fidelity is due to the low NA and relatively high background rate from scatter inherent in side-imaging. Crosstalk on neighboring PMT channels was not observed.

We note that the heating rate of the system is high compared to our previous work [24]. We think this is due to a combination of factors. For one, the ion could not be placed simultaneously on the rf null at an optimal position for Doppler cooling while maintaining good overlap with the clock laser waveguide output. As a result of the ion being off the rf null, it is more susceptible to amplifier noise in the trap rf, as well as excess micromotion. We believe that this is due to imperfect trap fabrication. A full three-dimensional characterization of this micromotion is planned for future work to rigorously establish the feasibility of this platform for precision optical clock operation.

Additional heating could also be due to the charging of the waveguides by the 369 nm beam. As stated in previous sections, we noticed a correlation between the input 369 nm laser power and compensation values of the dc electrodes used to position the ions in the 369 and 435 nm beams. The charging effect also suggests that the ions have additional exposure to the dielectric surfaces and an implied increase in Johnson noise heating [46]. This high heating rate prevents us from obtaining higher resolution with the Ramsey method and remains an improvement for future work.

The trapped ions are moved to their target locations within a site by adjusting the dc potentials. Each location needs a specific field profile due to small fabrication errors and localized charging effects. Most importantly, these profiles are tuned to achieve identical Rabi dephasing and $\pi/2$-pulse times. Therefore, we first used a dynamic solution to obtain precise control [24] and to optimize the compensation map for the trap. The dynamic solver provides a real-time calculation of the potential, which allows for easy compensation adjustment for various conditions. The dynamic solver allows for adjustment of a single trapping potential while maintaining the compensation fields at other trapping sites. The majority of tuning

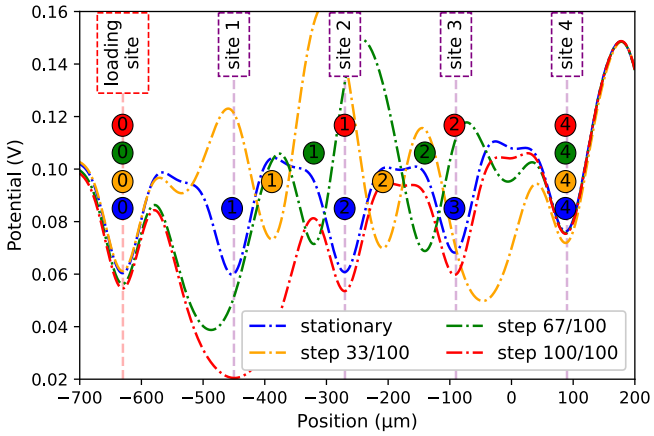


FIG. 5. A sample of the dc potential at the ions' height above the chip. Here, ions are shuttled from sites 1 and 2 to sites 2 and 3, respectively, to fill a vacancy at site 3. Ions at the loading site and site 4 remain stationary and have minimal perturbations to their respective dc axial trapping potentials. The minimums containing ions are labeled according to the site they originated from in the "stationary" case. The colors indicate the step to which they belong. Vertical dashed-lines mark the regions addressable by different waveguides. The loading region is marked with a red vertical dashed-line, while the clock sites are marked with purple vertical dashed-lines.

occurs along the trap axis, but the interplay of the dc and rf fields does not guarantee that the ion remains centered on the rf null. For the actual clock algorithm, the dc voltages are compiled into a discrete set to reduce computational load and to regularize the shuttling speed. All shuttling is done in the adiabatic regime. The shuttling moves ions between neighboring clock sites in less time than the clock cycle. Shuttling at this rate works to reduce perceived dead time in the clock cycle and reduces ion loss during the shuttling itself. Reducing the probability that the ion is lost during any shuttling attempt reduces the average number of attempts required to repopulate the furthest ions. Up to half of the ensemble ions are shuttled simultaneously to minimize the number of required shuttling steps while not blocking the probe of clock ions. For the specific case described in this paper, four different shuttling scenarios cover the replacement of ions at the clock sites. All scenarios begin and end with all potential wells present at all sites. Figure 5 shows an example of some steps in the compiled solution used in a single scenario. Step 0 is the state of all wells present at all sites. The number of shuttling scenarios is proportional to the number of ions, making this a conceivable path forward to managing large numbers of ions. The remaining limitations are the ion lifetimes, the tuning of individual sites, and the evolution of the stray field. These could be incorporated as part of a tuning procedure or possibly even dynamically adjusted for in more sophisticated algorithms. However, our stray field evolution did not occur on any meaningful timescale as long as 369 nm beam power remained nominal.

3. Side-imaging and signal optimization

A 2-inch objective lens with a NA of 0.12 was placed at the side window to exclusively capture maximum ion fluorescence while minimizing light noise from waveguide emissions. We placed extra pinholes of 100 μm diameter in front of the 1D array PMT (Hamamatsu H11659-200). Each pinhole was separated by 1 mm, equal to the pitch of the 1D PMT array. The image magnification was coarsely tuned by obtaining an image from a camera (Qimaging ROLERA em-c^2). With optimal alignment, we achieved a signal of > 2.5 kcps with $\approx$0.1 kcps of noise, an SNR greater than 25. This is about five times better than the SNR from our previous work [24], allowing us to decrease the detection time to 3 ms.

APPENDIX B: CLOCK INTERROGATION

1. Feedback

In a given clock cycle, the ensemble is probed at half the spectral linewidth from resonance shown in Fig. 6. In circumstances where the servo's tracked frequency is at the correct position, an individual ion will be shelved in the $^2D_{3/2}$ state 50% of the time for either probe. In the case where the servo's tracked frequency is not properly centered, one probe will be more likely to fluoresce in detection. This forms the basis of the error signal for the feedback. Two servo channels integrate the error signals obtained from interrogations on the left and right sides of the resonance, employing a locking scheme similar to established methods [43]. An example of the frequency displacement of these two second-order servos as they track the same ions is shown in Fig. 7. The interplay between the clock cycle length, the FWHM of the spectral line, and the first-order gain is the main contributor to our servo bandwidth of approximately 20 s (approximately 800 clock cycles). No additional probes are performed on or off resonance.

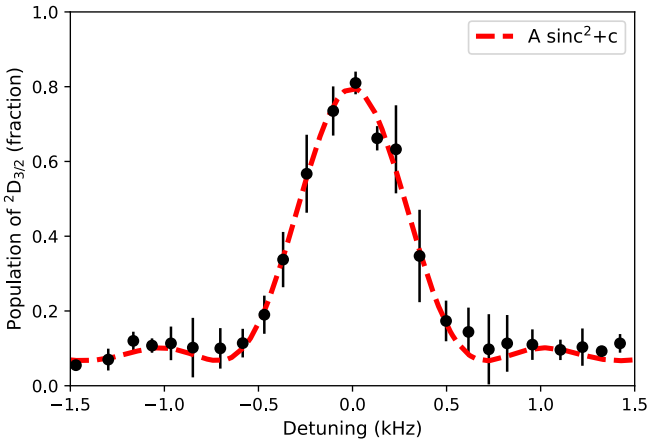


FIG. 6. Example spectrum the clock transition prior to running the clock. This provides the FWHM used in the servo.

2. Clock protocol

A single clock interrogation occurs in roughly 6 ms. The FPGA system that manages the optical modulation and readout of the clock algorithm is separate from the shuttling electronics. The shuttling electronics are unable to reliably receive messages, set up the voltages arrays in memory for the requested shuttle, execute a requested shuttle from the FPGA every clock cycle. To accommodate the shuttling electronics, the FPGA reports every 20 clock cycles ($\approx$0.47 s), while feedback still occurs every clock cycle. This information includes which ions are still present and additional data used for postprocessing and diagnostics. This time allows ions to go dark and subsequently return to the cooling cycle by collision if they go dark. If the ion is dark outside of the cooling cycle for a sufficient number of clock cycles, the ion is treated as lost and will be marked by the algorithm for reloading.

3. Systematics

In this work, we have focused on demonstrating clock operation and have not performed a detailed analysis of the systematic shifts and uncertainty of the absolute frequency. With regards to absolute frequency, the largest correction to consider was the second-order Zeeman shift. Through separate measurements, the correction from the second-order Zeeman shift was 19.026(64) kHz. The fit to the measurement to extract the shift used of literature values for the second-order Zeeman coefficient of the $m_f = 0$ transition, 0.5213 kHz/G^2 [48], and 0.84 MHz/G the first-order coefficient of the $m_f = \pm 1$ transitions. The precision is limited by the broader first-order Zeeman sensitive, $m_f = \pm 1$ transitions used to measure the local magnetic field. We attribute the frequency displacement drift in Fig. 7 largely to the ULE cavity stabilizing the local oscillator. An important observation from Fig. 4(b) is that

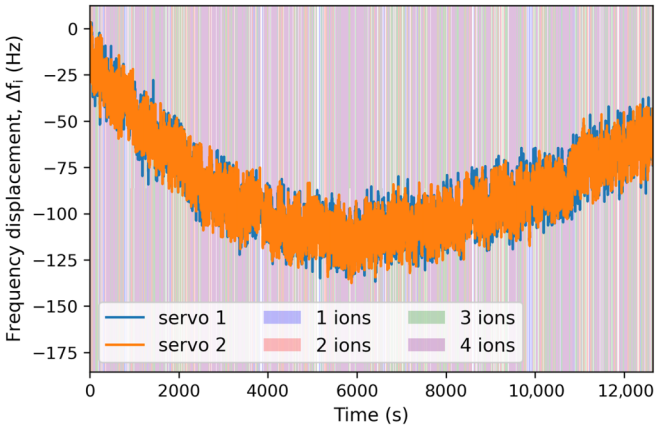


FIG. 7. An example of the two servos as they track the same ions. Colors above and below the mid-line indicate how many ions the algorithm claims to have. Each servo independently tracks the ions present for diagnostics.

the field uniformity is sufficient to not resolve a magnetic field gradient over the 540 μm that the clock sites occupy. The next contribution to corrections to the absolute frequency to be considered was a second-order Doppler shift. Adjusting the position of the ion to achieve similar Rabi rates, as in Fig. 4(a), carried inherent risk that the individual ions were moved off of the rf null, leading to additional micromotion. A simulation was used to estimate the rf null displacement, comparing the applied dc potential with one that would not have displaced the ions from the rf null. By this method, the overall second-order Doppler shift was estimated to be less in magnitude than −0.3 Hz. This effect may have been resolvable in Fig. 4(b) on a site-specific basis as some ions are displaced more than others in the simulation; however, its observation was greatly limited by the first-order servo error at 1.75 Hz. Additionally, there would be a black-body shift to the E2 transition of −0.35 Hz due to the room temperature vacuum chamber. Stability analysis and shifts shared by the clock sites would require an external frequency reference of adequate precision to better characterize.

[1] A. D. Ludlow, M. M. Boyd, J. Ye, E. Peik, and P. O. Schmidt, Optical atomic clocks, Rev. Mod. Phys. **87**, 637 (2015).

[2] N. Huntemann, C. Sanner, B. Lipphardt, C. Tamm, and E. Peik, Single-ion atomic clock with 3×10^{-18} systematic uncertainty, Phys. Rev. Lett. **116**, 063001 (2016).

[3] M. S. Safronova, D. Budker, D. DeMille, D. F. J. Kimball, A. Derevianko, and C. W. Clark, Search for new physics with atoms and molecules, Rev. Mod. Phys. **90**, 025008 (2018).

[4] S. M. Brewer, J.-S. Chen, A. M. Hankin, E. R. Clements, C. W. Chou, D. J. Wineland, D. B. Hume, and D. R. Leibrandt, $^{27}Al^+$ quantum-logic clock with a systematic uncertainty below 10^{-18}, Phys. Rev. Lett. **123**, 033201 (2019).

[5] M. C. Marshall, D. A. R. Castillo, W. J. Arthur-Dworschack, A. Aeppli, K. Kim, D. Lee, W. Warfield, J. Hinrichs, N. V. Nardelli, T. M. Fortier, J. Ye, D. R. Leibrandt, and D. B. Hume, High-stability single-ion clock with 5.5×10^{-19} systematic uncertainty, Phys. Rev. Lett. **135**, 033201 (2025).

[6] A. Chu, V. J. Martínez-Lahuerta, M. Miklos, K. Kim, P. Zoller, K. Hammerer, J. Ye, and A. M. Rey, Exploring the dynamical interplay between mass-energy equivalence, interactions, and entanglement in an optical lattice clock, Phys. Rev. Lett. **134**, 093201 (2025).

[7] E. A. Burt, J. D. Prestage, R. L. Tjoelker, D. G. Enzer, D. Kuang, D. W. Murphy, D. E. Robison, J. M. Seubert, R. T. Wang, and T. A. Ely, Demonstration of a trapped-ion atomic clock in space, Nature (London) **595**, 43 (2021).

[8] T. Lindvall *et al.*, Coordinated international comparisons between optical clocks connected via fiber and satellite links, Optica **12**, 843 (2025).

[9] E. Sheridan, N. J. Barton, R. Birrittella, V. Nehra, Z. Smith, C. Tison, A. M. Smith, S. Dharanibalan, V. Bedi, D. Hucul *et al.*, Telecommunications fiber-optic and free-space quantum local area networks at the air force research laboratory, arXiv:2508.01030.

[10] M. Takamoto, F.-L. Hong, R. Higashi, and H. Katori, An optical lattice clock, Nature (London) **435**, 321 (2005).

[11] M. M. Boyd, T. Zelevinsky, A. D. Ludlow, S. M. Foreman, S. Blatt, T. Ido, and J. Ye, Optical atomic coherence at the 1-second time scale, Science **314**, 1430 (2006).

[12] T. Bothwell, D. Kedar, E. Oelker, J. M. Robinson, S. L. Bromley, W. L. Tew, J. Ye, and C. J. Kennedy, JILA SrI optical lattice clock with uncertainty of 2.0×10^{-18}, Metrologia **56**, 065004 (2019).

[13] W. F. McGrew, X. Zhang, R. J. Fasano, S. A. Schäffer, K. Beloy, D. Nicolodi, R. C. Brown, N. Hinkley, G. Milani, M. Schioppo, T. H. Yoon, and A. D. Ludlow, Atomic clock performance enabling geodesy below the centimetre level, Nature (London) **564**, 87 (2018).

[14] C. W. Chou, D. B. Hume, J. C. J. Koelemeij, D. J. Wineland, and T. Rosenband, Frequency comparison of two high-accuracy Al^+ optical clocks, Phys. Rev. Lett. **104**, 070802 (2010).

[15] H. Hausser, J. Keller, T. Nordmann, N. Bhatt, J. Kiethe, H. Liu, I. Richter, M. Von Boehn, J. Rahm, S. Weyers *et al.*, $^{115}In^+$-$^{172}Yb^+$ Coulomb crystal clock with 2.5×10^{-18} systematic uncertainty, Phys. Rev. Lett. **134**, 023201 (2025).

[16] Z. L. Newman, V. Maurice, T. Drake, J. R. Stone, T. C. Briles, D. T. Spencer, C. Fredrick, Q. Li, D. Westly, B. R. Ilic *et al.*, Architecture for the photonic integration of an optical atomic clock, Optica **6**, 680 (2019).

[17] J. Chiaverini, R. B. Blakestad, J. Britton, J. D. Jost, C. Langer, D. Leibfried, R. Ozeri, and D. J. Wineland, Surface-electrode architecture for ion-trap quantum information processing, Quantum Inf. Comput. **5**, 419 (2005).

[18] D. Stick, W. K. Hensinger, S. Olmschenk, M. J. Madsen, K. Schwab, and C. Monroe, Ion trap in a semiconductor chip, Nat. Phys. **2**, 36 (2005).

[19] T. Rosenband and D. R. Leibrandt, Exponential scaling of clock stability with atom number, arXiv:1303.6357.

[20] M. G. Blain, R. Haltli, P. Maunz, C. D. Nordquist, M. Revelle, and D. Stick, Hybrid MEMS-CMOS ion traps for NISQ computing, Quantum Sci. Technol. **6**, 034011 (2021).

[21] J. Borregaard and A. S. Sørensen, Efficient atomic clocks operated with several atomic ensembles, Phys. Rev. Lett. **111**, 090802 (2013).

[22] V. S. S. Sundaram, E. Manfreda-Schulz, T. H. Stievater, N. F. Tyndall, T. Palone, V. Deenadayalan, C. Tison, Z. Smith, D. Hucul, G. A. Howland *et al.*, Highly-confined, low-loss visible photonics using foundry-fabricated silicon nitride circuits, in *CLEO: QELS_Fundamental Science*, San Jose, California (Optica Publishing Group, 2022), p. JTh3B–14, 10.1364/CLEO_AT.2022.JTh3B.14.

[23] A. R. Vasquez, C. Mordini, C. Vernière, M. Stadler, M. Malinowski, C. Zhang, D. Kienzler, K. K. Mehta, and J. P. Home, Control of an atomic quadrupole transition in a phase-stable standing wave, Phys. Rev. Lett. **130**, 133201 (2023).

[24] J. Kwon, W. J. Setzer, M. Gehl, N. Karl, J. Van Der Wall, R. Law, M. G. Blain, D. Stick, and H. J. McGuinness, Multi-site integrated optical addressing of trapped ions, Nat. Commun. **15**, 3709 (2024).

[25] K. K. Mehta, C. D. Bruzewicz, R. McConnell, R. J. Ram, J. M. Sage, and J. Chiaverini, Integrated optical addressing of an ion qubit, Nat. Nanotechnol. **11**, 1066 (2016).

[26] R. J. Niffenegger, J. Stuart, C. Sorace-Agaskar, D. Kharas, S. Bramhavar, C. D. Bruzewicz, W. Loh, R. T. Maxson, R. McConnell, D. Reens, G. N. West, J. M. Sage, and J. Chiaverini, Integrated multi-wavelength control of an ion qubit, Nature (London) **586**, 538 (2020).

[27] K. K. Mehta, C. Zhang, M. Malinowski, T.-L. Nguyen, M. Stadler, and J. P. Home, Integrated optical multi-ion quantum logic, Nature (London) **586**, 533 (2020).

[28] C. W. Hogle, D. Dominguez, M. Dong, A. Leenheer, H. J. McGuinness, B. P. Ruzic, M. Eichenfield, and D. Stick, High-fidelity trapped-ion qubit operations with scalable photonic modulators, npj Quantum Inf. **9**, 74 (2023).

[29] C. Noel, M. Berlin-Udi, C. Matthiesen, J. Yu, Y. Zhou, V. Lordi, and H. Häffner, Electric-field noise from thermally activated fluctuators in a surface ion trap, Phys. Rev. A **99**, 063427 (2019).

[30] J. M. Pino, J. M. Dreiling, C. Figgatt, J. P. Gaebler, S. A. Moses, M. S. Allman, C. H. Baldwin, M. Foss-Feig, D. Hayes, K. Mayer, C. Ryan-Anderson, and B. Neyenhuis, Demonstration of the trapped-ion quantum CCD computer architecture, Nature (London) **592**, 209 (2021).

[31] C. Mordini, A. Ricci Vasquez, Y. Motohashi, M. Müller, M. Malinowski, C. Zhang, K. K. Mehta, D. Kienzler, and J. P. Home, Multizone trapped-ion qubit control in an integrated photonics QCCD device, Phys. Rev. X **15**, 011040 (2025).

[32] W. Loh, J. Stuart, D. Reens, C. D. Bruzewicz, D. Braje, J. Chiaverini, P. W. Juodawlkis, J. M. Sage, and R. McConnell, A Brillouin laser optical atomic clock, arXiv:2001.06429.

[33] N. Chauhan, C. Caron, J. Wang, A. Isichenko, N. Helaly, K. Liu, R. J. Niffenegger, and D. J. Blumenthal, Trapped ion qubit and clock operations with a visible wavelength photonic coil resonator stabilized integrated Brillouin laser, arXiv:2402.16742.

[34] W. Loh, D. Reens, D. Kharas, A. Sumant, C. Belanger, R. T. Maxson, A. Medeiros, W. Setzer, D. Gray, K. DeBry, C. D. Bruzewicz, J. Plant, J. Liddell, G. N. West, S. Doshi, M. Roychowdhury, M. Kim, D. Braje, P. W. Juodawlkis, J. Chiaverini, and R. McConnell, Optical atomic clock interrogation via an integrated spiral cavity laser, arXiv:2403.12794.

[35] W. Loh, D. Reens, D. Kharas, A. Sumant, C. Belanger, R. T. Maxson, A. Medeiros, W. Setzer, D. Gray, K. DeBry, C. D. Bruzewicz, J. Plant, J. Liddell, G. N. West, S. Doshi, M. Roychowdhury, M. E. Kim, D. Braje, P. W. Juodawlkis, J. Chiaverini, and R. McConnell, Optical atomic clock interrogation using an integrated spiral cavity laser, Nat. Photonics **19**, 277 (2025).

[36] L. Chang, S. Liu, and J. E. Bowers, Integrated optical frequency comb technologies, Nat. Photonics **16**, 95 (2022).

[37] W. J. Setzer, M. Ivory, O. Slobodyan, J. W. Van Der Wall, L. P. Parazzoli, D. Stick, M. Gehl, M. G. Blain, R. R. Kay, and H. J. McGuinness, Fluorescence detection of a trapped ion with a monolithically integrated single-photon-counting avalanche diode, Appl. Phys. Lett. **119**, 154002 (2021).

[38] D. Reens, M. Collins, J. Ciampi, D. Kharas, B. F. Aull, K. Donlon, C. D. Bruzewicz, B. Felton, J. Stuart, R. J. Niffenegger, P. Rich, D. Braje, K. K. Ryu, J. Chiaverini, and R. McConnell, High-fidelity ion state detection using trap-integrated avalanche photodiodes, Phys. Rev. Lett. **129**, 100502 (2022).

[39] B. Hampel, D. H. Slichter, D. Leibfried, R. P. Mirin, S. W. Nam, and V. B. Verma, Trap-integrated superconducting nanowire single-photon detectors with improved rf tolerance for trapped-ion qubit state readout, Appl. Phys. Lett. **122**, 174001 (2023).

[40] M. Ivory, W. J. Setzer, N. Karl, H. McGuinness, C. DeRose, M. Blain, D. Stick, M. Gehl, and L. P. Parazzoli, Integrated optical addressing of a trapped ytterbium ion, Phys. Rev. X **11**, 041033 (2021).

[41] M. A. Uddin, M. Y. Ali, and H. Chan, Materials and fabrication issues of optical fiber array, Rev. Adv. Mater. Sci. **21**, 155 (2009), https://www.ipme.ru/e-journals/RAMS/no_22109/uddin1.html. https://www.researchgate.net/publication/228879692_Materials_And_Fabrication_Issues_Of_Optical_Fiber_Array

[42] T. R. Tan, C. L. Edmunds, A. R. Milne, M. J. Biercuk, and C. Hempel, Precision characterization of the $^2D_{5/2}$ state and the quadratic Zeeman coefficient in $^{171}Yb^+$, Phys. Rev. A **104**, L010802 (2021).

[43] E. Peik, T. Schneider, and C. Tamm, Laser frequency stabilization to a single ion, J. Phys. B **39**, 145 (2006).

[44] W. M. Itano, J. C. Bergquist, J. J. Bollinger, J. M. Gilligan, D. J. Heinzen, F. L. Moore, M. G. Raizen, and D. J. Wineland, Quantum projection noise: Population fluctuations in two-level systems, Phys. Rev. A **47**, 3554 (1993).

[45] N. V. Semenin, A. S. Borisenko, I. V. Zalivako, I. A. Semerikov, M. D. Aksenov, K. Y. Khabarova, and N. N. Kolachevsky, Determination of the heating rate and temperature of an ion chain in a linear Paul trap by the dephasing of Rabi oscillations, JETP Lett. **116**, 77 (2022).

[46] M. Teller, D. A. Fioretto, P. C. Holz, P. Schindler, V. Messerer, K. Schüppert, Y. Zou, R. Blatt, J. Chiaverini, J. Sage, and T. E. Northup, Heating of a trapped ion induced by dielectric materials, Phys. Rev. Lett. **126**, 230505 (2021).

[47] T. D. Morrison*et al.*, Autonomous multi-ion optical clock with on-chip integrated photonic light delivery, Zenodo home (2026), 10.5281/zenodo.23196108.

[48] R. M. Godun, P. B. R. Nisbet-Jones, J. M. Jones, S. A. King, L. A. M. Johnson, H. S. Margolis, K. Szymaniec, S. N. Lea, K. Bongs, and P. Gill, Frequency ratio of two optical clock transitions in $^{171}Yb^+$ and constraints on the time variation of fundamental constants, Phys. Rev. Lett. **113**, 210801 (2014).